IEEE Access
Multidisciplinary ⋮ Rapid Review ⋮ Open Access Journal

Received 11 February 2023, accepted 25 February 2023, date of publication 2 March 2023, date of current version 7 March 2023.

Digital Object Identifier 10.1109/ACCESS.2023.3251890

RESEARCH ARTICLE

Enhancement of Wireless Power Transfer for Automated Guided Vehicles Considering Disturbance Suppression

TSONG-SHING LEE[1], (Member, IEEE), SHYH-JIER HUANG[2], (Senior Member, IEEE), AND MING-JIA WU[2]

[1]Department of Electrical Engineering, Southern Taiwan University of Science and Technology, Tainan 71005, Taiwan
[2]Department of Electrical Engineering, National Cheng Kung University, Tainan 701, Taiwan

Corresponding author: Shyh-Jier Huang (clhuang@mail.ncku.edu.tw)

ABSTRACT This article proposes an enhanced wireless power transfer (WPT) for automated guided vehicles (AGVs) considering disturbance suppression. The study is motivated because existent resonant methods may induce unexpected disturbances, affecting the efficiency of power transfer and disturbing the voltage gain. This paper is, therefore, focused on the suppression of disturbances as well as the realization of an effective wireless power transmission. Moreover, by considering that the output voltage is often affected by misaligned charging, the system design has included the gain-frequency control along with an early detection of coil misalignment. It is anticipated that through this proposed approach, the constant-voltage output can be achieved while the efficiency of power transfer is improved as well. To validate the practicality of this approach, the hardware prototype is tested with a significant decrement of disturbance interference during the wireless power transmission, supporting the feasibility of the method for AGV charging applications.

INDEX TERMS Wireless power transfer, disturbance suppression, automated guided vehicle.

I. INTRODUCTION

Wireless power transfer (WPT) is increasingly applied to transportation applications that includes vehicular electrification, electric vehicles (EV), and automated guided vehicles (AGVs) [1], [2], [3], [4]. From the aspect of practical considerations, some studies have been devoted to investigating the power transfer between vehicles and grid, where grid-to-vehicle (G2V) and vehicle-to-grid (V2G) were both concerned [4], [5], [6], [7]. Yet, the induced harmonics or unexpected disturbances caused by mismatched parameters and various resonant topologies during WPT may appear and affect the operating performance.

To cope with such nuisances, previous studies have assessed different resonant compensation circuits [8], [9], [10], [11]. It was noted that the occurrence of mismatched parameters in the resonant architecture would induce current harmonics [12], [13], which was followed by the evaluation of generation source with signal analysis [13], [14], [15], [16]. Later on, the development of analytical methods and corresponding strategies were subsequently reported. Some studies quantified the impact of high-order harmonics based on the efficiency and circuit loss, while other studies focused on the investigation of control strategy, parameter tuning, and improved compensation [17], [18], [19]. The utilization of frequency modulation method was also reported to manage this issue [20], [21], [22], [23]. Encouraging results of the above methods may exhibit their effectiveness in the suppression of disturbances, yet each of them allows a further amendment in certain aspects.

Different from previous literatures, this article presents an enhanced WPT system embedded with the capability of disturbance suppression and constant-voltage control. The paper starts with the derivation of harmonic distortion and the analysis of resonance characteristics based on LCC-S compensation, by which the improved system design is prudently developed. A gain-frequency control that excels at maintaining a stable output voltage is also applied to cope with

The associate editor coordinating the review of this manuscript and approving it for publication was Chi-Seng Lam.

the problem of coil misalignment. Through this proposed circuit design, the system is verified with different tests to confirm its feasibility. To the best of our knowledge, this way of improved design and gain-frequency control with early misalignment-detection were not reported in the published literatures. Features of this method are threefold:

1) The study proposes a method of disturbance-suppression and develops a gain-frequency control for WPT, achieving a better performance for bidirectional wireless power transfer.
2) The proposed LCC-S resonant topology is systematically assessed, benefiting the justification of frequency-operating point and serving as useful reference for the controller design.
3) The system develops an early misalignment detection based on the gain-frequency control and presents the frequency hopping and regulating with high flexibility.

The rest of this article is organized as follows. Section II describes the proposed system with harmonics analysis and improved design, Section III analyzes the resonance characteristics with performance comparison, Section IV illustrates the flowchart with realization of gain-frequency control, Section V discusses the experimental results, and Section VI draws the conclusions.

II. PROPOSED SYSTEM

Fig. 1 delineates the block diagram of proposed WPT system for AGV applications. The power source side consists of dc input voltage V_U provided from grid-level power conditioner, a half-bridge converter, a T-type LCC resonant tank, and an inductive coil L_p. The AGV side composes an inductive coil L_s, capacitor C_s, a full-bridge converter, and charging network with battery storage devices. In this figure, the T-type LCC resonant tank is added with series capacitor C_s so as to form LCC-S circuit for impedance-matching compensation. The interactive coordination of bidirectional power transfer between V_U at grid and V_B at AGV side is also implemented. The coil L_s of AGV is placed at the upper side of coil L_p. The voltage V_B of storage device and the voltage V_U of power conditioner are coordinated to perform vehicle-to-grid (V2G) and grid-to-vehicle (G2V) power delivery. When the AGV operates at charging mode (G2V), the full-bridge converter acts as a rectifier to shape a dc voltage V_B from the voltage of v_{Ls} for subsequent AGV charging. Once the AGV operates at discharging mode (V2G), then the half-bridge converter acts as a voltage-doubling and the filter circuit forms a dc voltage V_U from inductive voltage of v_{Lp} for power conditioning at grid side. For both modes of charging and discharging, the suppression of harmonic disturbance and the preserving of voltage profile are both concerned. Description of circuit configuration and disturbance suppression are discussed in the following.

A. CIRCUIT CONFIGURATION

Fig. 2 illustrates the circuit configuration of the proposed system. The half-bridge converter and primary circuits

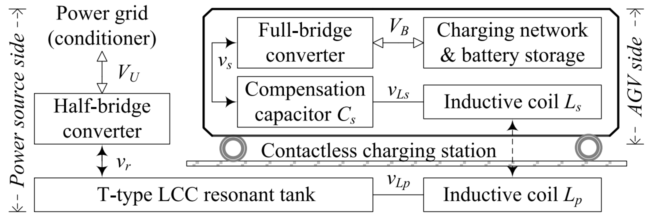

FIGURE 1. Block diagram of the proposed enhanced WPT systems.

(L_r, C_r, C_p, and L_p) are constructed at the power source side, and the full-bridge converter and secondary circuits (C_s and L_s) are formed as the storage source of AGV. The system adjusts the operating mode of half-bridge converter and full-bridge converter according to bidirectional power flow between V_U and V_B. The operating modes consist of 1) charging mode when starting the half-bridge converter and terminating the full-bridge converter and 2) discharging mode when terminating the half-bridge converter and starting the full-bridge converter.

In the control loop of Fig. 2, two sets of microcontroller units (TMS320F28335, Texas Instruments) are embedded to perform the gain-frequency regulation. The antenna chips (BC417143, Cambridge Silicon Radio) are employed for contactless serial data transmission. The feedback circuit detects the dc voltage of V_U and V_B individually at power source side and AGV side. The waveforms of current i_r and i_s are captured to justify if they are influenced by harmonics, while the coil misalignment is meanwhile detected. The frequency-hopping technique is employed here to control the driving signals of D_{g1}-D_{g2} and D_{g3}-D_{g6}, anticipating restricting the effects of harmonic disturbances.

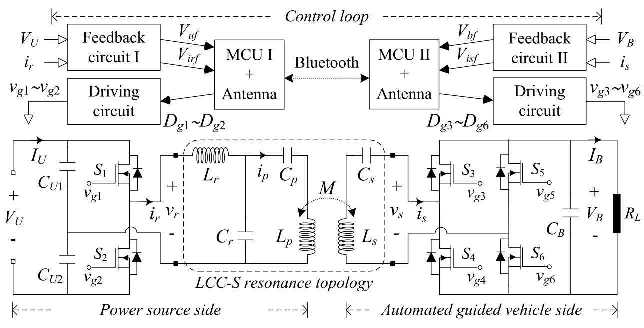

FIGURE 2. Circuit configuration of the bidirectional WPT systems.

Table 1 lists the specification of proposed system. In the circuit design, the gate-driven IC of HCPL-3120 (Avago Technologies) with bootstrap and photo-coupler isolation capability is adopted to convert D_{g1}-D_{g6} of 3.3 V to driving signals of v_{g1}-v_{g6} of 15 V. The driving signals are then employed to drive silicon carbide power MOSFETs S_1-S_6 (C2M0080120D, Cree Inc.), while the voltage V_U and V_B of two-terminals are stabilized for bidirectional power transfer.

Fig. 3 (a) shows the photograph of completed coil module, where the Litz wire with 500 strands of No. 40 AWG

TABLE 1. Specifications of the proposed system.

Specifications	Symbols	Values
Input voltage of grid side	V_U	400 V
Storage voltage of AGV side	V_B	120 V
Output power	P_o	400 W
Operation frequency	f_o	85 kHz
Air gap of coil module	g_r	100 mm

(0.08 mm diameter) is adopted. During the selection of this wire, it is noted that the skin depth of copper conductor is first calculated to be 0.226 mm under the frequency of 85 kHz (f_o) considering that the skin effect is related with the range of frequency. With such value of skin depth, the skin effect can be less concerned by employing the copper conductor of 40 AWG (0.08 mm diameter). The study meanwhile uses the Litz wire with 500 strands, with which the loading current is measured to be 6.85 A and the resistance amounts to 152 mΩ only. These measurements reveal that the selected conductor comes with sufficient ampacity along with reduced AC equivalent resistance. As seen from the figure, the size of coil L_p is 250 mm×250 mm (the inner diameter is 200 mm×200 mm) and that of coil L_s is 250 mm×250 mm (the inner diameter is 190 mm×190 mm). A ferrite core (the dimension is 300 mm×300 mm×3 mm) with a high relative permeability of 1500 is incorporated at the top of L_s pad and the bottom of L_p pad so as to reach a better coupling. It is worth noting that the diameter of transmitting coil is determined based on the given size of receiving pad of AGV, by which the coils of the same diameters at the transmitting and receiving side help to reach a satisfactory magnetic coupling. Meanwhile, a ferrite core pad of a bigger diameter is inserted here so that the coupling performance of mutual inductance can be better ensured.

Fig. 3 (b) shows the photograph of the completed hardware circuit of WPT system, including power converters, resonant inductors and capacitors, MCU controller, driving circuit, coil module, and dummy load. Table 2 lists the specification of coil module, detailing the coil design of enhanced WPT platform for guided vehicles applications. Note that for the proposed system, the equivalent coil resistances r_p and r_s of L_p and L_s are measured to be 152 mΩ with the operating frequency of 85 kHz. The quality factor is computed to be 407, which is deemed useful to decrease the power loss and improve the efficiency of power delivery.

TABLE 2. Specifications of the coil module.

Specifications	Symbols	Values
coil inductance of power side	L_p	116.1 μH
coil inductance of AGV side	L_s	117.4 μH
Mutual inductance	M	36.9 μH
Coupling coefficient	k	0.318

B. ANALYSIS OF HARMONIC DISTURBANCES

Since the harmonics can be deemed as a kind of disturbance, this section focuses on the analysis of harmonic components

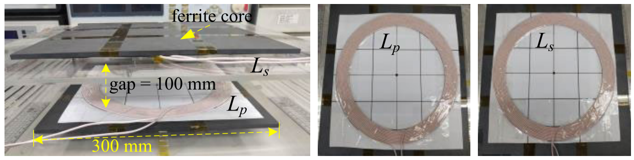

(a)

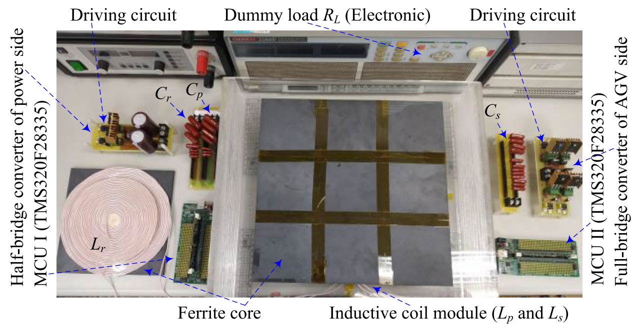

(b)

FIGURE 3. Photographs of the (a) inductive coil module and (b) hardware circuit realization.

of bidirectional power transfer based on LCC-S resonant circuit. The relationship between total harmonic distortion and resonance parameters are derived to quantify the influence of harmonics. Fig. 4 depicts the equivalent T-type model of LCC-S resonant circuit under charging mode. At this time, the voltage V_U of power supply is converted to v_{rG} by half-bridge converter, hence inducing the voltage of v_{sG} to deliver power to rectifier and filter circuits for AGV charging, where R_s is the equivalent load of rectifier, filter circuit, and charging network R_L. The study expresses the voltage of $v_{rG}(t)$ as Fourier series:

$$v_{rG}(t) = \frac{2V_U}{\pi} \sum_{n=1,3,....}^{\infty} \frac{1}{n} \sin(2\pi n f_s t) \tag{1}$$

Then the voltage-current relation is arranged as a matrix form below

$$\begin{bmatrix} v_{rG} \\ 0 \\ 0 \end{bmatrix} = \begin{bmatrix} Z_r & -Z_c & 0 \\ -Z_c & Z_p & -Z_m \\ 0 & -Z_m & Z_s + R_s \end{bmatrix} \begin{bmatrix} i_{rG} \\ i_{pG} \\ i_{sG} \end{bmatrix} \tag{2}$$

where the resonance impedances are expressed as

$$Z_c = \frac{1}{j\omega C_r}, Z_m = j\omega M, \text{ and } Z_s = j\omega L_s + \frac{1}{j\omega C_s}$$
$$Z_p = j\omega L_p + \frac{1}{j\omega C_r} + \frac{1}{j\omega C_p}, \text{ and } Z_r = j\omega L_r + \frac{1}{j\omega C_r}$$

Following the inversion of matrix inversion, the loop current of equivalent circuit can be derived as

$$i_{rG} = \frac{v_{rG}}{Z_{inG}} = \frac{v_{rG}[Z_m^2 - Z_p(Z_s + R_s)]}{Z_r[Z_m^2 - Z_p(Z_s + R_s)] + Z_c^2(Z_s + R_s)} \tag{3}$$

$$i_{pG} = \frac{-v_{rG} Z_c (Z_s + R_s)}{Z_r[Z_m^2 - Z_p(Z_s + R_s)] + Z_c^2(Z_s + R_s)} \tag{4}$$

$$i_{sG} = \frac{-v_{rG} Z_m Z_c}{Z_r[Z_m^2 - Z_p(Z_s + R_s)] + Z_c^2(Z_s + R_s)} \tag{5}$$

From equation (3), the input impedance Z_{inG} becomes

$$Z_{inG} = \frac{v_{rG}}{i_{rG}} = Z_r + \frac{Z_c^2(Z_s + R_s)}{Z_m^2 - Z_p(Z_s + R_s)} \tag{6}$$

Since the input voltage v_{rG} is of square waveform, the i_{rG} fed into the LCC-S resonant circuit would come with higher-order harmonics. The fundamental component and multiple-order harmonic components of i_{rG} are calculated as follows:

$$I_{rGn} = \left|\frac{v_{rG}(n\omega_s)}{Z_{inG}(n\omega_s)}\right| = \frac{2V_{\mathrm{U}}}{n\pi}\frac{1}{|Z_{inG}(n\omega_s)|},\ n = 1, 3, 5, \ldots \tag{7}$$

Therefore, when AGV operates at charging mode, the total harmonic distortion THD_G of current i_{rG} is written as

$$\begin{aligned}\mathrm{THD}_G &= \frac{\sqrt{I_{rG3}^2 + I_{rG5}^2 + \ldots}}{I_{rG1}} \\ &= |Z_{inG}(\omega_s)|\sqrt{\sum_{n=3,5,\ldots}^{\infty}\frac{1}{|nZ_{inG}(n\omega_s)|^2}}\end{aligned} \tag{8}$$

Equation (8) indicates that the high-order harmonics can be suppressed through the increased impedance Z_{inG} of LCC-S resonant circuit. Meanwhile, equation (6) also reveals that the increment of inductance L_r would help restrict the unexpected influences of current harmonics. Now since the i_{sG} is related to impedance Z_c as expressed in (5), the influence of high-order harmonics can be ignored. Therefore, based on the theory of first harmonic approximation (FHA), the voltage V_B at the battery side under the charging mode is written as

$$V_B = \frac{V_U}{2}\left|\frac{Z_m Z_c R_s}{Z_r[Z_m^2 - Z_p(Z_s + R_s)] + Z_c^2(Z_s + R_s)}\right|\ \omega = \omega_s \tag{9}$$

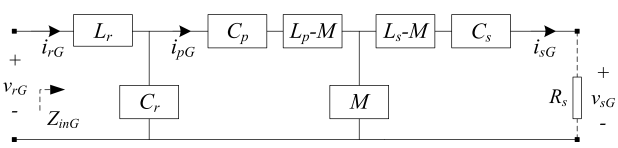

FIGURE 4. Equivalent T-model of the LCC-S circuit under the charging mode.

Fig. 5 depicts the equivalent T-type model of LCC-S resonant circuit under discharging mode, where v_{sV} and i_{sV} are input voltage and current provided from full-bridge converter, v_{rV} and i_{rV} are voltage and current fed into double-voltage rectifier, and R_r is the equivalent load of the double-voltage rectifier and grid-side network at the front stage. In Fig. 5, $v_{sV}(t)$ can be expressed as Fourier series

$$v_{sV}(t) = \frac{4V_B}{\pi}\sum_{n=1,3,\ldots.}^{\infty}\frac{1}{n}\sin(2\pi nf_s t) \tag{10}$$

The voltage-current relation can be arranged as below

$$\begin{bmatrix} v_{sV} \\ 0 \\ 0 \end{bmatrix} = \begin{bmatrix} Z_s & -Z_m & 0 \\ -Z_m & Z_p & -Z_c \\ 0 & -Z_c & Z_s + R_r \end{bmatrix}\begin{bmatrix} i_{sV} \\ i_{pV} \\ i_{rV} \end{bmatrix} \tag{11}$$

After the inversion of matrix, the loop current of equivalent circuit becomes

$$i_{sV} = \frac{v_{sV}}{Z_{inV}} = \frac{v_{sV}[Z_c^2 - Z_p(Z_r + R_r)]}{Z_s[Z_c^2 - Z_p(Z_r + R_r)] + Z_m^2(Z_r + R_r)} \tag{12}$$

$$i_{pV} = \frac{-v_{sV}Z_m(Z_r + R_r)}{Z_s[Z_c^2 - Z_p(Z_r + R_r)] + Z_m^2(Z_r + R_r)} \tag{13}$$

$$i_{rV} = \frac{-v_{sV}Z_m Z_c}{Z_s[Z_c^2 - Z_p(Z_r + R_r)] + Z_m^2(Z_r + R_r)} \tag{14}$$

From equation (12), the input impedance Z_{inV} is expressed as

$$Z_{inV} = \frac{v_{sV}}{i_{sV}} = Z_s + \frac{Z_m^2(Z_r + R_r)}{Z_c^2 - Z_p(Z_r + R_r)} \tag{15}$$

The fundamental and multiple-order harmonics as well as the THD_V of current i_{sV} are calculated as follows

$$\begin{aligned}I_{sVn} &= \left|\frac{v_{sV}(n\omega_s)}{Z_{inV}(n\omega_s)}\right| \\ &= \frac{4V_B}{n\pi}\frac{1}{|Z_{inV}(n\omega_s)|},\ n = 1, 3, 5, \ldots\end{aligned} \tag{16}$$

$$\begin{aligned}\mathrm{THD}_V &= \frac{\sqrt{I_{sV3}^2 + I_{sV5}^2 + \ldots}}{I_{sV1}} \\ &= |Z_{inV}(\omega_s)|\sqrt{\sum_{n=3,5,\ldots}^{\infty}\frac{1}{|n \cdot Z_{inV}(n\omega_s)|^2}}\end{aligned} \tag{17}$$

Analysis results of (17) indicate that the increment of total impedance Z_{inV} promotes the suppression capability of higher order harmonics. It is also noted that the Z_{inV} is mainly affected by the inductance L_s rather than the L_r, and equation (14) reveals that the i_{rV} is related to impedance Z_c. Through the aforementioned theoretical derivations, they conclude that the increased values of inductance L_r and coil L_s are helpful to suppress harmonic disturbances based on the analysis results of equations (8) and (17).

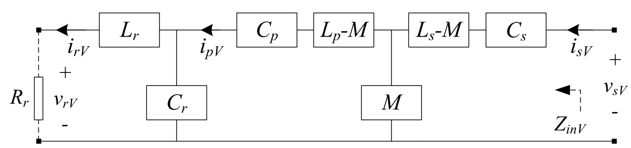

FIGURE 5. Equivalent T-model of LCC-S circuit under discharging mode.

C. DERIVATION OF IMPROVED RESONANCE CIRCUIT

Fig. 6 shows the equivalent circuit of LCC-S resonance topology, where parameters of compensation capacitance C_r, C_s, and C_p are designed as below

$$C_r = \frac{1}{\omega_s^2 L_r},\ C_s = \frac{1}{\omega_s^2 L_s},\ \text{and}\ C_p = \frac{1}{\omega_s^2(L_p - L_r)} \tag{18}$$

By assuming that the impedance-matching is achieved via (18), the voltage gain G_v of LCC-S resonance circuit from v_r to v_s can be simplified as

$$G_v = |v_s/v_r| = M/L_r \tag{19}$$

Equation (19) indicates that the voltage gain G_v of Fig. 6 is related with mutual inductance M and inductance L_r. Hence, if L_r is adjusted to increase the input impedance, then the G_v will be varied to tune the output voltage. Note that the C_s and C_p of (18) are affected by the coil inductance, revealing that the capability of disturbance suppression can be enhanced via the increased L_p and L_s, yet this way may simultaneously increase the coil size and affect the impedance network characteristics. Therefore, this paper proposes an improved resonance design supplemented by LCC-S architecture in anticipation of increasing the design flexibility. This improved design starts with the observation of Fig. 6 based on Kirchhoff's voltage law, by which loop equations are individually expressed as

$$v_r = j(\omega L_r - \frac{1}{\omega C_r})i_r + j(\frac{1}{\omega C_r})i_p \tag{20}$$

$$j\omega M i_s = j(\omega L_p - \frac{1}{\omega C_r} - \frac{1}{\omega C_p})i_p + j(\frac{1}{\omega C_r})i_r \tag{21}$$

$$j\omega M i_p = [j(\omega L_s - \frac{1}{\omega C_s}) + R_s]i_s \tag{22}$$

When the operation frequency of ω_o is equal to resonance frequency of ω_s with the coefficient of i_p of (21) amounting to zero, then the following equations are obtained

$$\omega_s L_p - \frac{1}{\omega_s C_r} - \frac{1}{\omega_s C_p} = 0 \text{ and } i_s = \frac{1}{\omega_s^2 C_r M} i_r \tag{23}$$

Since the $v_r i_r$ is equal to $v_s i_s$ based on the principle of energy conservation, voltage gain of G_v can be further derived as

$$G_v = |v_s/v_r| = |i_r/i_s| = \omega_s^2 C_r M \tag{24}$$

Equation (24) shows that the voltage gain G_v and load R_s are mutually independent, implying that the constant-voltage output can be well maintained during load change. Besides, since this voltage gain G_v is unaffected by L_r, the current disturbances can be effectively filtered out by increasing the design value of L_r. The capacitor C_r and C_p can be derived from (23) and (24) as

$$C_r = \frac{G_v}{\omega_s^2 M} \text{ and } C_p = \frac{1}{\omega_s^2[L_p - (M/G_v)]} \tag{25}$$

Then the C_s is calculated when ω_0 is equal to ω_s by assuming that the imaginary part of $Z_{tol}(\omega_s)$ amounts to zero, which is expressed as

$$C_s = \frac{1}{\omega_s^2(G_v^2 L_r + L_s - G_v M)} \tag{26}$$

Table 3 lists the comparisons of designed parameters between conventional and proposed approaches. In this table, the conventional method is seen restricted by system specifications, yet the proposed approach comes with a flexible way of tuning the compensating inductance L_r while the gain G_v is stably maintained. In other words, following the calculation of C_r and C_p based on the specification of Table 1 and the coil module of Table 2 for the comprehension of voltage transfer gain G_v, then the proposed method would be able to compute C_s once the L_r is determined by referring the disturbance suppression results of Figs. 7 and 8, thus completing the parameter design of the resonant circuit design.

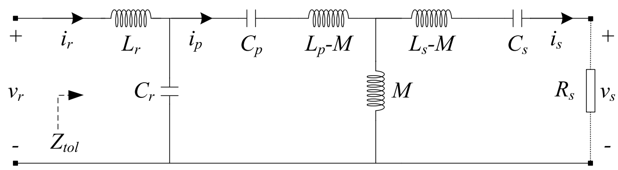

FIGURE 6. Equivalent circuit of LCC-S resonant topology.

TABLE 3. Comparison of designed parameters.

Symbols	Conventional	Proposed
G_v	M/L_r	$\omega_s^2 C_r M$
C_r	$1/\omega_s^2 L_r$	$G_v/\omega_s^2 M$
C_p	$1/[\omega_s^2(L_p\text{-}L_r)]$	$1/[\omega_s^2(L_p\text{-}M/G_r)]$
C_s	$1/\omega_s^2 L_s$	$1/[\omega_s^2(G_v^2 L_r\text{+}L_s\text{-}G_v M)]$
L_r	M/G_v	Depend on system's requirement

D. DETERMINATION OF RESONANT PARAMETERS

The study next goes to determine the inductance L_r in the improved design. Based on the tabulations of Table 1 and 3 under different values of L_r and P_o, Fig. 7 depicts the total harmonic distortion THD$_G$ and THD$_V$ of resonance currents i_r and i_s. In Fig. 7(a), the curves indicate that the THD$_G$ of current i_r gradually decreases with respect to the increased L_r. Then, Fig. 7(b) reveal that the THD$_V$ of current i_s comes with a smaller variation when compared to that of Fig. 7(a). The main reason lies in that the input impedance Z_{inV} is less increased when the inductance of L_r is mapped to the secondary side of AGV, and the LCC-S resonant topology does not have an external inductance to increase Z_{inV} during discharging. These simulation results are in good agreement with theoretical derivation of Section II-B.

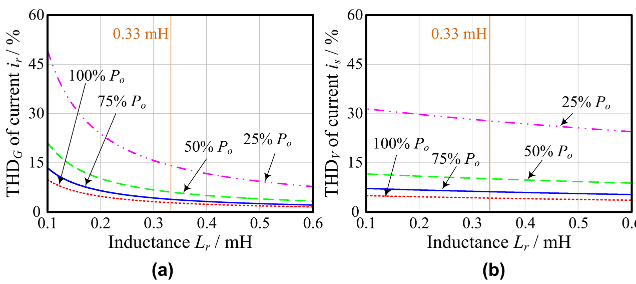

FIGURE 7. Simulation results of THD under different output power P_o at (a) charging and (b) discharging mode.

Fig. 8 illustrates the simulation curves of capacitor voltage versus L_r under different P_o conditions. The curves indicate that the voltage stress of capacitor C_r grows with the increased L_r and P_o. Considering that the cost of capacitor increases with a larger L_r, this study selects the inductance of 0.33 mH for L_r, in which the THD of resonance currents can be restricted to be lower than 14.1% under all P_o at charging mode while the peak-to-peak value of capacitor C_r stress is restricted below 1.17 kV. This way of design needs less component cost with a better suppression of disturbance.

To summarize the aforementioned calculation and analysis process in a systematic way, Fig. 9 depicts the flowchart of design procedure of proposed method. The flowchart starts with the root cause of disturbance generation, which is followed by the determination of resonant parameters C_r, G_v, C_s, and L_r based on the predetermined voltage gain of G_v. Parameters of L_r and C_r are then tuned according to the analysis results of Figs. 7-8, hence paving the road to grasp the disturbance suppression and component stress. For example, based on the specification of Table 1, the proposed method first determines the voltage gain G_v of 0.6 for the proposed WPT system. Then, the C_r and C_p are computed to be 56.7 nF and 64.6 nF based on the data of Table 2 and 3, respectively. Therefore, with the predetermined L_r of 0.33 mH as reported by the plots of Figs 7 and 8, the C_s is calculated to be 16.5 nF. This completes the system design process, by which all the parameters of LCC-S resonance circuit are summarized in Table 4. Conclusively, the proposed design exhibits several features that include (1) the achievement of enhanced disturbance suppression, 2) the systematic calculations of voltage gain with comparisons, and 3) the determination of circuit parameters.

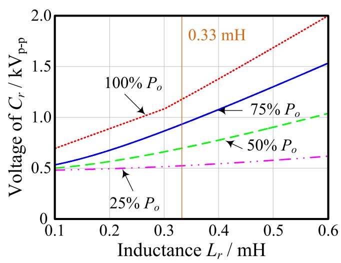

FIGURE 8. Simulation results of capacitor voltage stress with different L_r and P_o.

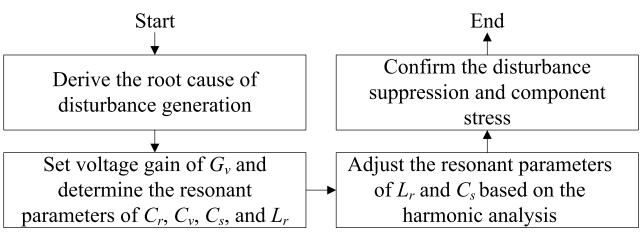

FIGURE 9. Flowchart of systematic design procedure.

III. RESONANCE CHARACTERISTICS INVESTIGATION

This section examines resonance behaviors of LCC-S topology using the proposed design, where the voltage output and gain-frequency trend under charging and discharging are investigated. Based on tabulations of Table 4, the capability of disturbance suppression using proposed mechanism is compared to that using the conventional method. Figs. 10 and 11 show the simulation results of THD with conventional and proposed mechanism under charging and discharging modes. The conventional design shown in Fig. 10(a) indicates that the value of THD_G is higher than 85% at light output power of 25% P_o, causing an increased current stress of MOSFET and additional conduction loss. Yet, from the proposed design of Fig. 10(b), the THD_G is decreased with the increased P_o, which manifests that the proposed method improves the disturbance suppression and reduces the power loss. The curves of Fig. 11 further indicate that the overall THD_V of the proposed method is lower than that of conventional design, confirming the achievement of disturbance suppression. These plots reveal that the proposed system has a stable voltage output, validating the design simplification and control realization.

TABLE 4. Specifications of resonance components.

Specifications	Symbol	Conventional / Proposed
Resonance inductance	L_r	61.8 μH / 330 μH
Resonance capacitance	C_r	56.6 nF / 56.7 nF
Primary capacitance	C_p	64.7 nF / 64.6 nF
Secondary capacitance	C_s	30.0 nF / 16.5 nF

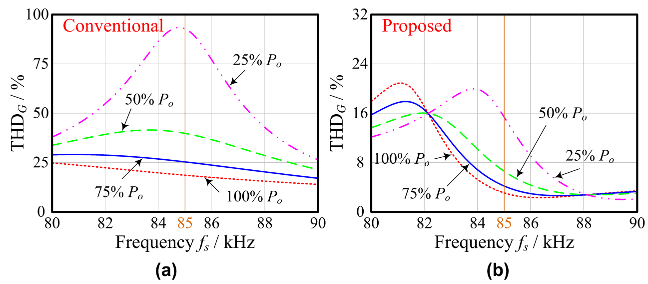

FIGURE 10. Simulation results of THD_G as a function of frequency f_s with (a) conventional and (b) proposed design under charging mode.

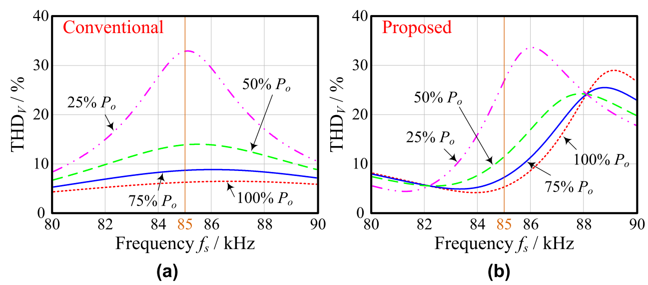

FIGURE 11. Simulation results of THD_V as a function of frequency f_s with (a) conventional and (b) proposed design under discharging mode.

The study next investigates the output voltage V_B and V_U under different P_o when a coil is misaligned with the charging station. Fig. 12 delineates the simulation results of voltage V_B and V_U under various P_o. When the system is operated at f_s of 85 kHz, the figure shows that V_B and V_U are not deviated with the change of P_o, supporting the exhibition of constant-voltage characteristics under charging and discharging modes. This varying trend of gain can be adopted as a reference for frequency tracking.

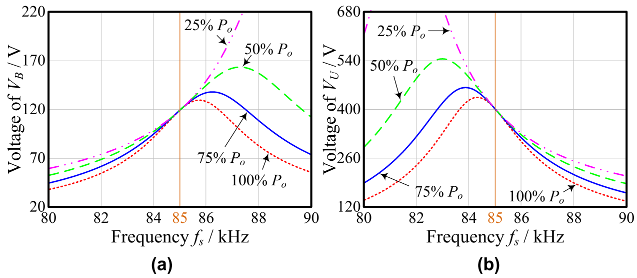

FIGURE 12. Simulation results of (a) voltage V_B and (b) voltage V_U as a function of frequency f_s under charging mode and discharging mode.

Subsequently, a 40% coil misalignment is concerned, which is the maximum misalignment of coil L_s encountered in our AGV station. For the simulation of this 40% misalignment, the k is found to reduce from 0.318 down to 0.253 when the coil moves from the aligned place to a misalignment of 90 mm. Fig. 13 illustrates the simulated curves of voltage V_B and V_U with 100% P_o and 90 mm misalignment. In Fig. 13(a), the conventional design presents a low output voltage that requires a wider range of frequency regulation to increase the voltage V_B, failing to meet system requirements. On the other hand, the curve using the proposed method can adjust the voltage level via frequency regulation. In Fig. 13(b), the simulation results show that the conventional design exhibits an excessively high voltage output and cause a large current flow into the grid; yet the proposed method effectively stabilizes the output voltage V_U via frequency control.

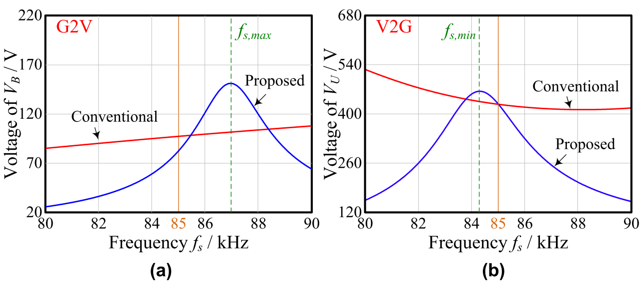

FIGURE 13. Simulation results of (a) voltage V_B and (b) voltage V_U as a function of frequency f_s when system operated with 100% P_o and coil misalignment of 90 mm.

Figs. 14 and 15 delineate the simulated curves of voltage (V_B and V_U) and total harmonic distortion (THD_G and THD_V) with respect to different coupling coefficients of k. In Fig. 14, the curves illustrate the alignment case with k of 0.318 as well as the 90 mm misalignment with k of 0.253. The direction of frequency modulation is grasped for both operation modes based on the varying trend of curves. It means that the operating frequency f_o is swiftly adjusted along the direction of high frequency when the pulse frequency modulation (PFM) module of MCU receives the triggering signals of f_{t-u} or f_{t-b}.

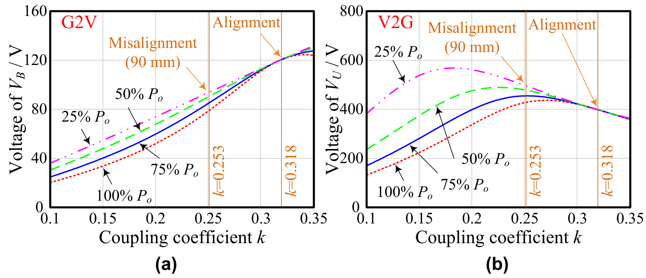

FIGURE 14. Simulation results of (a) V_B and (b) V_U as a function of k when operated with different P_o.

In Fig. 15, the curves indicate that THD_G and THD_V are decreased with the increased f_o when k is gradually reduced. The level of disturbance can be better restricted with the assistance of frequency-regulation control. In this study, by considering voltage stability and disturbance suppression, the operating frequency point f_{setG} of 86.0 kHz and f_{setV} of 85.4 kHz are deemed suitable when individually operated at charging and discharging mode. These values of f_{setG} and f_{setV} can be adopted as frequency-hopping points of controller. Based on these simulations, several features are observed that include 1) the proposed method maintains the stability of output voltage with limited disturbances, 2) the voltage deviations can be amended via gain-frequency adjustment, and 3) the controller design is systematically presented with simplification.

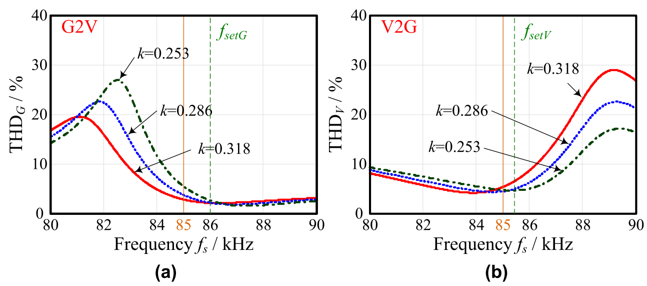

FIGURE 15. Simulation results of (a) THD_G and (b) THD_V as a function of f_s when operated with 100% P_o and different k.

IV. CONTROL STRATEGIES

This section is aimed to investigate the misalignment detection as well as frequency regulation, by which the voltage variation is effectively restricted. Procedures of control strategies are discussed as follows.

A. MISALIGNMENT DETECTION AND GAIN-FREQUENCY CONTROL

Fig. 16 depicts the block diagram of gain-frequency control. The controller helps tune the operating frequency f_o such that the output voltage is swiftly stabilized during the coil misalignment. In the figure, the microcontroller unit (MCU) includes timer module, analog to digital converter (ADC), digital filter, pulse frequency modulation (PFM), output comparator, and core processor with control algorithm. The feedback circuit I and II are responsible for signal acquisition of current (i_r and i_s) and voltages (V_U and V_B). After converting these signals of i_r, i_s, V_U, and V_B to those of V_{irf}, V_{isf}, V_{uf}, and V_{bf}, they are delivered to both MCUs to perform the misalignment detection and constant-voltage control. The voltages of V_U and V_B are grasped based on real-time measurements and closed-loop control via communication antenna, where the slopes of current waveforms (i_r and i_s) are served as reference for scenario indicator of coil misalignment. This way of signal indicator is motivated since the coil misalignment often causes current harmonics, and these harmonics are highly related with the slope variation of current waveform. The comprehension of the change of slope is useful for the forewarning of coil misalignment.

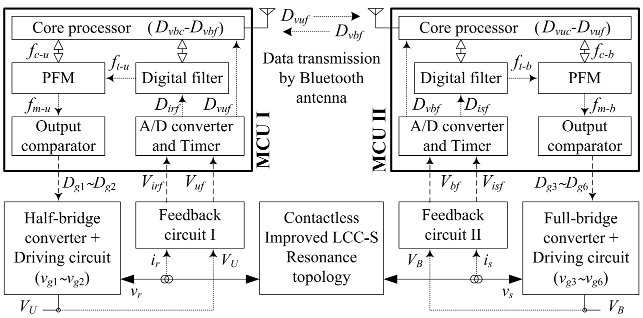

FIGURE 16. Block diagram of gain-frequency control.

B. CONTROLLING OF OUTPUT STABILITY

Fig. 17 shows the flowchart of gain-frequency control. The system starts to determine the operation mode with the initial frequency of f_{st} of 85 kHz, where the hopping frequency of f_{setG}, f_{estV} as well as the operating frequency ranging from $f_{s,min}$ to $f_{s,max}$ is given. This is followed by the detection of resonance current of i_r and i_s served as the reference for alerting if the receiving coil is misaligned. Once any misalignment happens, the system will perform the frequency-hopping to tune the f_o to the predetermined values of f_{setG} and f_{estV} in order to suppress the disturbances. Meanwhile, the V_U at grid side and the V_B at AGV side are continuously detected with the regulation of f_o of inverter. On the other hand, if there is no misalignment detected, then the controller goes to observe the voltage difference of ΔV in order to comprehend the disparity between feedback signals (D_{vuf} and D_{vbf}) and command signals (D_{vuc} and D_{vbc}). Subsequently, the controller pays attention to the frequency of f_o. Only when the f_o is situated within the operable region, then the controller would adjust the frequency and ensures a better voltage stability.

V. EXPERIMENTAL RESULTS

To assess the feasibility of the proposed system to suppress the disturbance and maintain the constant voltage output, different scenarios are conducted. Detailed tests and results are discussed below.

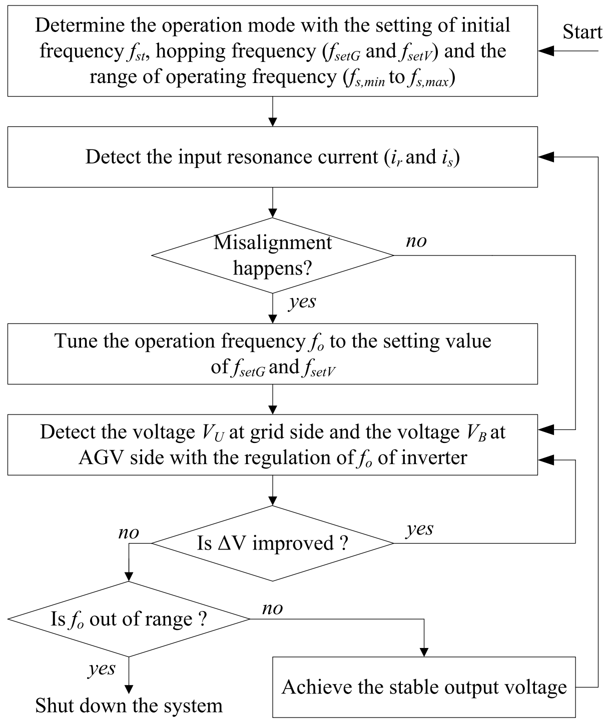

FIGURE 17. Flowchart of gain-frequency control.

A. DISTURBANCE SUPPRESSION OF RESONANCE CURRENT

In this test, the frequency components of resonance current are examined using conventional design and proposed design. A voltage V_U of 400 V (grid side) is applied with the battery voltage V_B of 120 V (AGV side) for bidirectional power transfer. The voltage (v_r and v_s) and current (i_r and i_s) under charging and discharging mode are measured. Figs. 18 and 19 shows the measured results of v_r and i_r when the system operated at 50% P_o of 200 W and 100% P_o of 400 W under charging mode. Figs. 18(a) and 19(a) show that the resonance current i_r contains plentiful harmonic disturbances when operated with conventional design, and Figs. 18(b) and 19(b) indicate that the current disturbance is largely suppressed via the proposed design. Next, when the system is operated under discharging mode, Fig. 20 shows the measured results of v_s and i_s when operated at P_o of 200 W and 400 W, validating that the proposed design effectively reduces the current disturbances during discharging. Table 5 and 6 lists the improved results based on measured waveforms. For both charging and discharging modes of operation, the tabulations of Table 5 and 6 reveal that the peak value and THD are reduced significantly using the proposed method when compared to the conventional one. Moreover, through the data analysis and comparisons, the simulation results of Fig. 10 and Fig. 11 are close to experimental results of Table 5 and Table 6. For example, for the charging mode with P_o of 300 W, both simulations and experiments indicate that the THD of i_r is 3.9%, revealing the feasibility and practicality of systemic design procedure for disturbance suppression.

These plots and tabulations support the feasibility of proposed method on disturbance suppression of resonance current during bidirectional wireless power transfer.

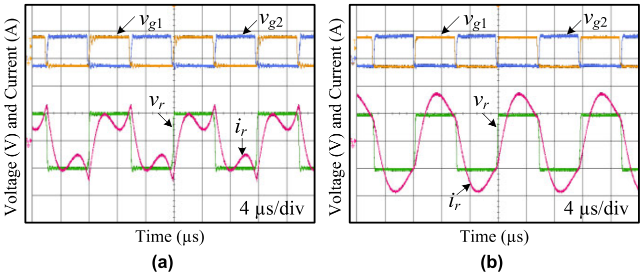

FIGURE 18. Measured waveforms of v_r and i_r with (a) conventional design and (b) proposed design when operated at output power P_o of 200 W. (v_{g1}-v_{g2}: 20 V/div, v_r: 200 V/div, i_r: 2 A/div-(a), and i_r: 1 A/div-(b)).

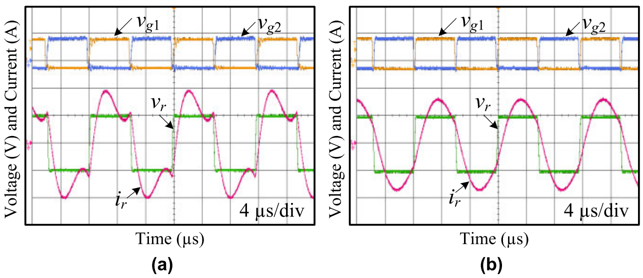

FIGURE 19. Measured waveforms of v_r and i_r with (a) conventional design and (b) proposed design when operated at output power P_o of 400 W. (v_{g1}-v_{g2}: 20 V/div, v_r: 200 V/div, and i_r: 2 A/div).

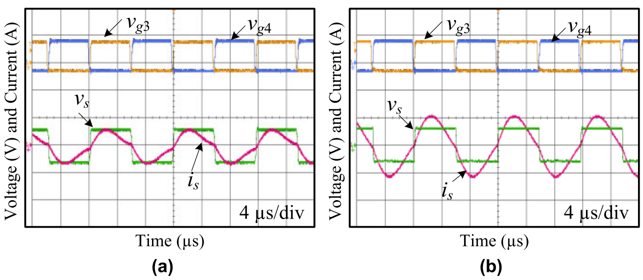

FIGURE 20. Measured waveforms of v_s and i_s with proposed design when operated at output power P_o of (a) 200 W and (b) 400 W. (v_{g3}-v_{g4}: 20 V/div, v_s: 200 V/div, and i_s: 5 A/div).

TABLE 5. Improved results under charging mode.

P_o (W)	Conventional method Peak value / THD of i_r	Proposed method Peak value / THD of i_r
100	2.32 A_{P-P} / 94.8 %	0.67 A_{P-P} / 12.9 %
200	2.64 A_{P-P} / 47.2 %	1.78 A_{P-P} / 5.2 %
300	2.81 A_{P-P} / 41.0 %	2.53 A_{P-P} / 3.9 %
400	3.92 A_{P-P} / 31.6 %	3.41 A_{P-P} / 2.9 %

B. PERFORMANCE COMPARISON OF POWER TRANSMISSION

In this test, the voltage stability and power transfer efficiency without gain-frequency control using conventional and proposed design scheme are compared. The voltage V_U of 400 V and V_B of 120 V are individually given with output power of P_o ranging from 80 W to 400 W. Fig. 21 shows the measured waveforms of output voltage and current when operated at charging and discharging mode. As shown in Fig. 21(a), V_B and I_B are 119.2 V and 3.37 A provided from V_U through inductive power transfer, by which the P_o for AGV charging network is 400 W and the error of ΔV is 0.67%. In Fig. 21(b), V_U and I_U is measured about 397.4 V and 1.01 A when operated at the discharging mode. These test results confirm that voltages of V_B and V_U are well maintained during bidirectional WPT.

TABLE 6. Improved results under discharging mode.

P_o (W)	Conventional method Peak value / THD of i_s	Proposed method Peak value / THD of i_s
100	1.45 A_{P-P} / 38.5 %	1.32 A_{P-P} / 25.4 %
200	3.02 A_{P-P} / 17.2 %	2.92 A_{P-P} / 10.2 %
300	4.21 A_{P-P} / 12.3 %	4.12 A_{P-P} / 7.2 %
400	5.28 A_{P-P} / 8.6 %	5.23 $_{P-P}$ / 4.8 %

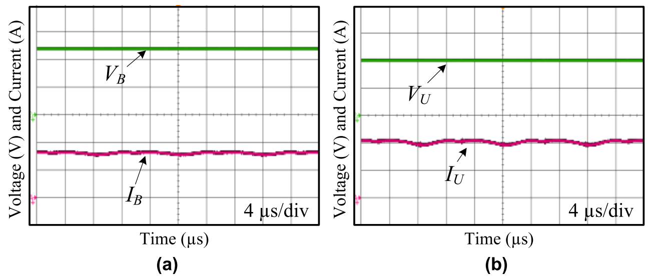

FIGURE 21. Measured waveforms of V_B, V_U, I_B, and I_U with the output power P_o of 400 W under (a) charging mode and (b) discharging mode. (V_B: 50 V/div, V_U: 200 V/div, I_B: 2 A/div, and I_U: 0.5 A/div).

Figs. 22 and 23 show the experimental results of output voltage and system efficiency of η_{ub} and η_{bu} at different P_o using conventional method and proposed approach. In Figs. 21-23, the curves indicate that the proposed method presents stable output voltages of V_B and V_U with higher transmission efficiencies of η_{ub} and η_{bu}. Both voltages of V_B and V_U are stabilized at 120V and 400V when operated at different output power conditions. By comparing these experimental results with simulation results of Fig. 12, they are seen to be consistent, validating the transfer gain G_v and constant-voltage characteristics are well behaved.

C. VALIDATION OF GAIN-FREQUENCY CONTROL

In this test, the voltage stability and transfer efficiency with and without gain-frequency control under coil misalignment are closely observed. Figs. 24 and 25 show the test results of voltage and efficiency under light load of 100 W and heavy load of 400 W. In Fig. 24(a) and 24(c), when the system is operated at 100 W and 400 W without control, the V_B is gradually reduced following the increased misalignment distance. Yet, with the assistance of gain-frequency control, the V_B can be maintained at approximately 120 V under different

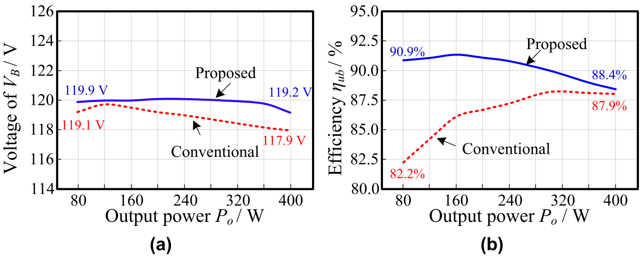

FIGURE 22. Measured results of (a) voltage V_B and (b) transmission efficiency η_{ub} with respect to output power P_o under charging mode.

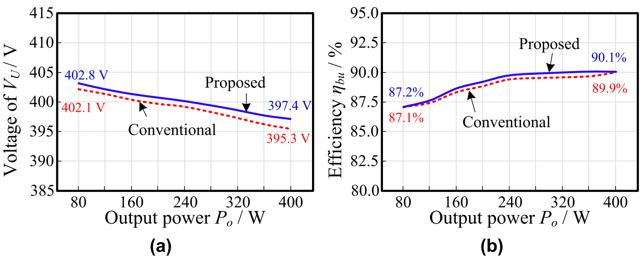

FIGURE 23. Measured results of (a) voltage V_U and (b) power transmission efficiency η_{bu} with respect to output power P_o under discharging mode.

misalignments. For example, when the system is operated at P_o of 400 W with misalignment of 90 mm, the voltage V_B is improved from 80.1 V to 119.8 V. Such improvement can be also found in Fig. 24(b) and Fig. 24(d), where the efficiency η_{ub} is raised up to 90.3% and 86.9% under 90 mm misalignment with P_o of 100 W and 400 W.

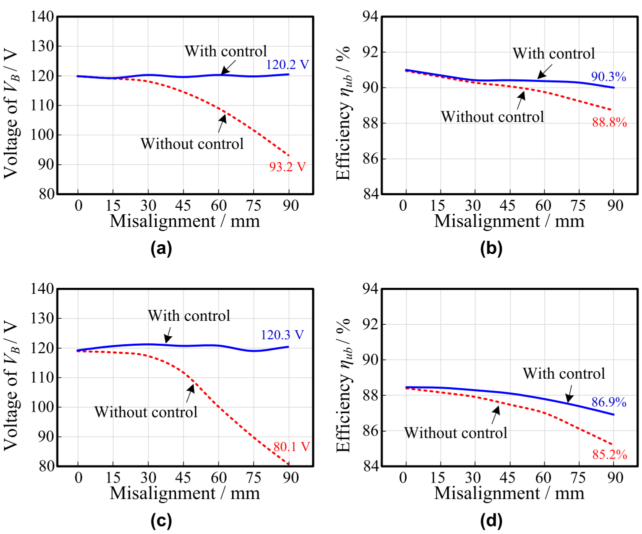

FIGURE 24. Measured results of the (a) V_B and (b) η_{ub} with P_o of 100 W, and the (c) V_B and (d) η_{ub} with P_o of 400 W under charging mode.

Next, when the system is situated at the discharging more, Fig. 25(a) and 25(c) indicates that V_U is maintained at approximately 400 V with less variation than the one without the support of gain-frequency control. The gain-frequency control trend of experimental results of Fig. 25 is in good

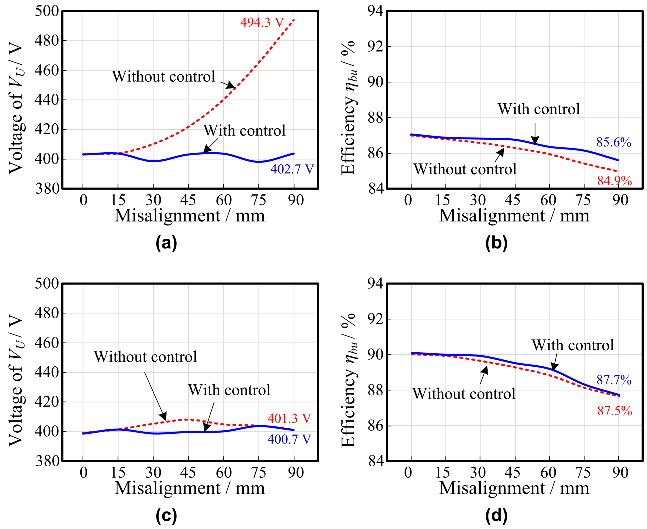

FIGURE 25. Measured results of (a) V_U and (b) η_{bu} with P_o of 100 W, and the (c) V_U and (d) η_{bu} with P_o of 400 W under discharging mode.

agreement with that of simulations results of Figs. 13-15. Meanwhile, as seen from Fig. 25(b) and 25(d), the plots demonstrate that the efficiency is improved to 85.6% and 87.7% with P_o of 100 W and 400 W. Experiences gained from these practical tests are useful for WPT-based AGV applications.

VI. CONCLUSION

This paper presents a disturbance suppression technique along with the gain-frequency control for WPT-based AGV systems. Derivation of bidirectional power transfer and the evaluation of disturbance are individually made based on LCC-S resonant circuit accompanying with improved parameter design, resonance characteristics simulation, and simplified control strategies. Experimental results confirm that the proposed approach effectively tunes the operating frequency, improves the efficiency of power transfer, achieves the stabilized output voltage, and enhances the capability of disturbance suppression. Test outcomes gained from this study own the potential of extending to automated guided vehicles with storage and retrieval applications.

REFERENCES

[1] A. Babaki, S. Vaez-Zadeh, and A. Zakerian, "Performance optimization of dynamic wireless EV charger under varying driving conditions without resonant information," *IEEE Trans. Veh. Technol.*, vol. 68, no. 11, pp. 10429–10438, Nov. 2019.

[2] D. H. Tran, V. B. Vu, and W. Choi, "Design of a high-efficiency wireless power transfer system with intermediate coils for the on-board chargers of electric vehicles," *IEEE Trans. Power Electron.*, vol. 33, no. 1, pp. 175–187, Jan. 2018.

[3] M. G. S. Pearce, G. A. Covic, and J. T. Boys, "Reduced ferrite double d pad for roadway IPT applications," *IEEE Trans. Power Electron.*, vol. 36, no. 5, pp. 5055–5068, May 2021.

[4] A. A. S. Mohamed and O. Mohammed, "Physics-based co-simulation platform with analytical and experimental verification for bidirectional IPT system in EV applications," *IEEE Trans. Veh. Technol.*, vol. 67, no. 1, pp. 275–284, Jan. 2018.

[5] S. Weearsinghe, D. J. Thrimawithana, and U. K. Madawala, "Modeling bidirectional contactless grid interfaces with a soft DC-link," *IEEE Trans. Power Electron.*, vol. 30, no. 7, pp. 3528–3541, Jul. 2015.
[6] H. Zeng, S. Yang, and F. Z. Peng, "Design consideration and comparison of wireless power transfer via harmonic current for PHEV and EV wireless charging," *IEEE Trans. Power Electron.*, vol. 32, no. 8, pp. 5943–5952, Aug. 2017.
[7] L. Wang, U. K. Madawala, and M.-C. Wong, "A wireless vehicle-to-grid-to-home power interface with an adaptive DC link," *IEEE J. Emerg. Sel. Topics Power Electron.*, vol. 9, no. 2, pp. 2373–2383, Apr. 2021.
[8] S. Ruddell, U. K. Madawala, and D. J. Thrimawithana, "A wireless EV charging topology with integrated energy storage," *IEEE Trans. Power Electron.*, vol. 35, no. 9, pp. 8965–8972, Sep. 2020.
[9] L. Yang, X. Li, S. Liu, Z. Xu, and C. Cai, "Analysis and design of an LCCC/S-compensated WPT system with constant output characteristics for battery charging applications," *IEEE J. Emerg. Sel. Topics Power Electron.*, vol. 9, no. 1, pp. 1169–1180, Feb. 2021.
[10] J. Feng, Q. Li, F. C. Lee, and M. Fu, "LCCL-LC resonant converter and its soft switching realization for omnidirectional wireless power transfer systems," *IEEE Trans. Power Electron.*, vol. 36, no. 4, pp. 3828–3839, Apr. 2021.
[11] H.-L. Jou, J.-C. Wu, K.-D. Wu, and C.-Y. Kuo, "Bidirectional DC–DC wireless power transfer based on LCC-C resonant compensation," *IEEE Trans. Power Electron.*, vol. 36, no. 2, pp. 2310–2319, Feb. 2021.
[12] F. Lu, H. Zhang, C. Zhu, L. Diao, M. Gong, W. Zhang, and C. C. Mi, "A tightly coupled inductive power transfer system for low-voltage and high-current charging of automatic guided vehicles," *IEEE Trans. Ind. Electron.*, vol. 66, no. 9, pp. 6867–6875, Sep. 2019.
[13] L. He and D. Guo, "A clamped and harmonic injected class-E converter with ZVS and reduced voltage stress over wide range of distance in WPT system," *IEEE Trans. Power Electron.*, vol. 36, no. 6, pp. 6339–6350, Jun. 2021.
[14] Y. Fang and B. M. H. Pong, "Multiple harmonics analysis for variable frequency asymmetrical pulsewidth-modulated wireless power transfer systems," *IEEE Trans. Ind. Electron.*, vol. 66, no. 5, pp. 4023–4030, May 2019.
[15] Y. Fang, B. M. H. Pong, and R. S. Y. Hui, "An enhanced multiple harmonics analysis method for wireless power transfer systems," *IEEE Trans. Power Electron.*, vol. 35, no. 2, pp. 1205–1216, Feb. 2020.
[16] F. Lu, Y. Zhang, H. Zhang, C. Zhu, L. Diao, M. Gong, W. Zhang, and C. Mi, "A low-voltage and high-current inductive power transfer system with low harmonics for automatic guided vehicles," *IEEE Trans. Veh. Technol.*, vol. 68, no. 4, pp. 3351–3360, Apr. 2019.
[17] J. Zhang, Z. He, A. Luo, Y. Liu, G. Hu, X. Feng, and L. Wang, "Total harmonic distortion and output current optimization method of inductive power transfer system for power loss reduction," *IEEE Access*, vol. 8, pp. 4724–4736, 2020.
[18] W. Xu, K. W. Chan, S. W. Or, S. L. Ho, and M. Liu, "A low-harmonic control method of bidirectional three-phase Z-Source converters for vehicle-to-grid applications," *IEEE Trans. Transport. Electrific.*, vol. 6, no. 2, pp. 464–477, Jun. 2020.
[19] Y. Yao, Y. Wang, X. Liu, F. Lin, and D. Xu, "A novel parameter tuning method for a double-Sided LCL Compensated WPT system with better comprehensive performance," *IEEE Trans. Power Electron.*, vol. 33, no. 10, pp. 8525–8536, Oct. 2018.
[20] Y. Zhang, T. Kan, Z. Yan, and C. C. Mi, "Frequency and voltage tuning of series–series compensated wireless power transfer system to sustain rated power under various conditions," *IEEE J. Emerg. Sel. Topics Power Electron.*, vol. 7, no. 2, pp. 1311–1317, Jun. 2019.
[21] G. Guidi and J. A. Suul, "Minimizing converter requirements of inductive power transfer systems with constant voltage load and variable coupling conditions," *IEEE Trans. Ind. Electron.*, vol. 63, no. 11, pp. 6835–6844, Nov. 2016.
[22] C. Zhao and D. Costinett, "GaN-based dual-mode wireless power transfer using multifrequency programmed pulse width modulation," *IEEE Trans. Ind. Electron.*, vol. 64, no. 11, pp. 9165–9176, Nov. 2017.
[23] Y. Jiang, L. Wang, Y. Wang, J. Liu, M. Wu, and G. Ning, "Analysis, design, and implementation of WPT system for EV's battery charging based on optimal operation frequency range," *IEEE Trans. Power Electron.*, vol. 34, no. 7, pp. 6890–6905, Jul. 2019.

TSONG-SHING LEE (Member, IEEE) received the Ph.D. degree in electrical engineering from National Cheng Kung University, Tainan, Taiwan, in 2015. He worked with AU Optronics Corporation, Hsinchu, Taiwan, from 2004 to 2016. Since 2016, he has been with the Department of Electrical Engineering, Southern Taiwan University of Science and Technology, Tainan, where he is currently a Professor. His research interests include power electronic converters, inductively coupled power transfer systems, display power supply, resonant circuit, and piezoelectric transformer power applications.

SHYH-JIER HUANG (Senior Member, IEEE) received the Ph.D. degree in electrical engineering from the University of Washington, Seattle, in 1994. He is currently a distinguished Professor with the Department of Electrical Engineering, National Cheng Kung University, Tainan, Taiwan. His current research interests include energy conversion, industrial electronics, and signal-processing applications. He won the Outstanding Research Award from the National Science Council of Taiwan, in 2004, the Outstanding Electrical Engineering Professor Award from the Chinese Institute of Electrical Engineering, in 2005, and the Outstanding Technical Achievement Award from the IEEE Tainan Section, in 2016. He served as the IEEE Taipei Chapter Chair for the IEEE Power Engineering Society, from 2002 to 2003.

MING-JIA WU was born in New Taipei City, Taiwan, in 1996. He received the B.S. and M.S. degrees in electrical engineering from the National Cheng Kung University, Tainan, Taiwan, in 2019 and 2020, respectively. He is currently with Macroblock Inc., Taiwan. His research interests include power electronics, wireless power transfer, and firmware system for power supply development.